Publications of the Astronomical Society of Australia (2026), **43**, e074, 15 pages
doi:10.1017/pasa.2026.10208

CAMBRIDGE UNIVERSITY PRESS

Research Article

Constraining FRB microstructure with polarised shot noise

Joel C. F. Balzan[1], Apurba Bera[1,2], Clancy W. James[1] and Bradley W. Meyers[3,1]

[1]The International Centre for Radio Astronomy Research (ICRAR), Curtin University, Bentley, WA, Australia, [2]ASTRON, Netherlands Institute for Radio Astronomy, Dwingeloo, Netherlands and [3]Australian SKA Regional Centre (AusSRC), Curtin University, Bentley, WA, Australia

Abstract

We present FIRES, a polarised shot-noise (PSN) framework that models fast radio burst (FRB) dynamic spectra as the incoherent superposition of Gaussian microshots with varying polarisation angles (PAs). Applied to the CRAFT bursts FRB 20191001A and FRB 20240318A, FIRES can reproduce key spectro-polarimetric behaviours seen in these data: scattering suppresses PA variability on the trailing edge, while the leading edge preferentially retains intrinsic structure when sufficient signal-to-noise is present. We quantify this behaviour using the PA variance ratio $\mathcal{R}_\psi$ and explore the joint plane of measured linear polarisation fraction Π_L versus PA variance to identify allowed regions of microshot number N, intrinsic PA dispersion σ_ψ, and intrinsic linear fraction $\Pi_{L,0}$ at fixed signal-to-noise. This restricts these combinations permitted within the adopted shot-noise framework. For FRB 20191001A, the data are consistent with an extended parameter space, reflecting degeneracies between intrinsic PA structure, microshot superposition, scattering, finite sampling, noise, and the assumed microshot-property distributions. FRB 20240318A occupies a more restricted region, favouring fewer microshots and larger intrinsic PA dispersion. By combining an emission-mechanism-independent forward-modeling framework with minimal assumptions and observational constraints, FIRES facilitates qualitative and quantitative exploration of how microshot superposition, scattering, finite sampling, and noise can shape observed FRB polarimetry under the PSN model.

Keywords: Fast radio bursts (FRBs); polarisation; interstellar scattering; radio transients

(Received 27 January 2026 UTC; revised 14 May 2026 UTC; accepted 18 May 2026 UTC)

1. Introduction

Fast radio bursts (FRBs) are transient radio signals characterised by their short duration and high brightness temperatures (Lorimer et al. 2007). The FRB population is diverse, exhibiting various properties such as apparent 'one-off ' events or strong repeaters (see Petroff et al. 2019, 2022, for recent reviews), highly variable polarisation angles (PAs), linear and circular polarisation fractions, rotation measures (RMs), as well as complex temporal and spectral profiles with multiple peaks and varying widths (e.g. Sherman et al. 2024; Sand et al. 2025; Scott et al. 2025). The study of these structures is essential for deciphering FRB generation mechanisms and the media through which they propagate.

FRBs show diverse PA behaviour. Only one FRB is well fit by a rotating vector model (RVM; Mckinven et al. 2025), a characteristic of a rotating neutron star, with circumstantial evidence for two more (Bera et al. 2024). Attempts to fit RVMs to a large population of repeater bursts show that some are well fit; however, their results are inconsistent with each other (Liu et al. 2025). Other FRBs show a variety of PA swings (Luo et al. 2020), or apparently flat PA profiles (e.g. Pandhi et al. 2024). The Canadian Hydrogen Mapping Experiment (CHIME) and the Deep Synoptic Array 110 (DSA-110) previously catagorised FRBs by their spectro-temporal morphology (Pleunis et al. 2021; Sand et al. 2025), the smooth PA evolution measured across the burst envelope (Pandhi et al. 2024) and their polarisation fractions (Sherman et al. 2024). These are highly dependent on S/N, time resolution, and propagation effects and leads to arbitrary classifications as suggested by Scott et al. (2025). Studying burst-envelope-scale PA behaviour may be useful for identifying rotational signatures or probing large-scale, spatially averaged magnetic field structure, and can inform us of potential progenitors; however, it may provide limited insight into the rapid local plasma processes that generate the emission, which may arise either in the magnetosphere (e.g. Lu & Kumar 2018) or in more distant outflow/shock regions (e.g. Lyubarsky 2014).

Scott et al. (2025) present high-time-resolution (HTR) polarisation properties of 35 FRBs from the Commensal Real-time ASKAP Fast Transients (CRAFT) Incoherent-Sum Survey (Shannon et al. 2025). They move away from previous classifications, showing that all FRBs likely have multiple components and have intrinsically variable PAs. However, measuring these temporal structures can be influenced by several factors, including the intrinsic properties of the source and its environment, and particularly scattering along the line of sight. When sampled with HTR, FRBs with little-to-no scattering and high signal-to-noise (S/N) can exhibit complex, narrow intrinsic widths (nanoseconds–microseconds; Nimmo et al. 2022) and highly variable PAs within the burst envelope (e.g. Gupta et al. 2022; Snelders et al. 2023; Scott et al. 2025). Observations of these structures can place stringent constraints on the size of the emitting region and emission mechanisms of FRBs, as well as the various propagation media (e.g. Beniamini & Kumar 2020).

The idea of radio pulses being comprised of multiple smaller 'shots' was first suggested by Rickett (1975) in the

Corresponding author: Joel C. F. Balzan, Email: joel.balzan@icrar.org.

Cite this article: Balzan Joel C. F., Bera A, James CW and Meyers BW. (2026) Constraining FRB microstructure with polarised shot noise. *Publications of the Astronomical Society of Australia* **43**, e074, 1–15. https://doi.org/10.1017/pasa.2026.10208

© The Author(s), 2026. Published by Cambridge University Press on behalf of Astronomical Society of Australia. This is an Open Access article, distributed under the terms of the Creative Commons Attribution licence (https://creativecommons.org/licenses/by/4.0/), which permits unrestricted re-use, distribution and reproduction, provided the original article is properly cited.

amplitude-modulated noise model for pulsars. This idea was extended by Cordes (1976) who implemented polarisation variations to explain short-time scale polarisation structures, the so-called 'polarised shot noise' (PSN) model. Many further developments have since been made to the model to account for stochastic processes (e.g. Melrose & Macquart 1998; McKinnon 2006; Osłowski et al. 2011). The most famous application of the shot-models is to the Crab pulsar, which displays nanosecond duration shots (nanoshots) with PA microstructure (Hankins & Eilek 2007; Hankins et al. 2016). Nimmo et al. (2022) and Scott et al. (2025) similarly note that their FRB samples have structures resembling Crab nanoshots.

Of the Crab pulsar's many components, single pulses in the main pulse and interpulse exhibit similar polarimetric nanostructure to FRBs. They often appear substantially depolarised at time resolutions of order tens of μs to ms, but at nanosecond time resolution and with minimal scattering they resolve into 100% polarised nanoshots with random PAs (Hankins et al. 2015, 2016). Though, the PA variability of these very bright pulses observed at HTR can be affected by self-noise and small-number statistics when the averaging is insufficient (van Straten 2009). Hankins et al. (2016) show that unresolved microbursts generally have highly disordered PA profiles, consistent with shots having random PAs. Occasionally, their PAs show ordered swings (see their Figure 4), which may trace underlying plasma or magnetic field structures from the emission environment. They also show that microbursts are in fact unresolved collections of narrowband nanoshots, with some demonstrating substructures of timescales less than 4 ns (see their Figure 8). This behaviour is consistent with expectations from the PSN model. Giant pulses (GPs) are a subclass of single pulses with luminosities several orders of magnitude greater than the average pulses, a distinct energy distribution (power law), and a narrow emission phase window (compared to the average pulse profile). In terms of duration and energetics, Crab GPs and their underlying nanoshot mechanism are the most analogous phenomena to FRBs (e.g. Nimmo et al. 2022). These Crab phenomena each show intense PA variability on nanosecond to microsecond timescales (e.g. Jessner et al. 2010; Hankins et al. 2016) and a variety of spectro-temporal morphologies, on durations similar to FRBs observed at very-high time resolution.

A natural question is whether depolarisation in FRBs may arise from the superposition of many microshots, analogous to the behaviour of Crab microbursts. Other contributors include depolarisation from scattering, Faraday rotation through turbulent media, or the intrinsic emission mechanism itself. Disentangling these possibilities requires controlled forward modelling of FRB microstructure and polarisation at HTR. However, the current sample of high-S/N, low-scatter FRBs with nanosecond-microsecond resolution remains limited, motivating the need for realistic simulations.

Several existing packages offer pulsar-signal simulation capabilities (e.g. Hotan et al. 2004; Hazboun et al. 2021), but these are generally unsuited to FRBs because they model emission profiles with simple Gaussian components and lack polarisation-analysis tools. In this paper, we introduce the Fast, Intense Radio Emission Simulator (`FIRES`),[a] a Python package for simulating and analysing FRB dynamic spectra under the PSN model. We describe `FIRES`, and demonstrate how `FIRES` can reproduce key observed FRB properties,including PA variance, depolarisation, and linear polarisation fractions, show how microshot superposition can naturally generate the diversity of polarimetric structures seen in FRBs, and show to what extent FRB parameters can be constrained.

[a]https://github.com/JoelBalzan/FIRES.

2. Modelling dynamic spectra

Following the idea that all FRBs intrinsically have multiple components (Scott et al. 2025), we model the dynamic spectra of FRBs as a superposition of Gaussian microshots with different PAs (Cordes 1976) using `FIRES`. Each microshot is defined by its amplitude, time of arrival (TOA), width, PA, and polarisation fractions, with the latter specifying that each microshot is partially elliptically polarised. For our initial model, we assume that each microshot has a Gaussian intensity profile with a peak amplitude sampled from a power law distribution, consistent with Crab GP energetics (e.g. Bera & Chengalur 2019). In principle, a degeneracy exists between the number of shots and their amplitudes: an alternative model could instead assume a constant number of shots whose amplitudes vary to reproduce the envelope. The amplitude distribution of Crab nanoshots does seem consistent with a power law (e.g. Figure 8 from Hankins et al. 2016); however, this has not yet been quantitatively constrained (see Appendix C.1 for a comparison of amplitude distribution power laws).

We further assume that their TOAs are distributed normally, and we ignore frequency dependence in intrinsic power. Given the high linear polarisation of FRBs and commonly assumed neutron star magnetospheric emission models (e.g. Lu & Kumar 2018), we adopt a picture in which the emitting magnetic field is predominantly ordered with only small perturbations. We therefore sample microshot PAs from a normal distribution. Each microshot has its full-width half-maximum (FWHM) sampled from a uniform distribution, and all other parameters are fixed. The microshots are then scattered by convolution with a thin-screen scattering response, diffractive interstellar scintillation (DISS) is applied as a multiplicative gain field, and noise is added to create realistic FRB dynamic spectra. `FIRES` can apply Faraday rotation and PA trends, however, we do not use them here. The list of parameters used in the model are presented in Table 1.

The Stokes I dynamic spectrum, comprised of N microshots in time t (ms) and frequency ν (MHz), is

$$D_I[t,\nu] = \left[\sum_{i=1}^{N} A_i \exp\left(-\frac{(t-t_i)^2}{2\sigma_{w,i}^2}\right)\right] * h_\nu(t), \qquad \sigma_{w,i} = \frac{w_i}{2\sqrt{2\log 2}},$$

where $*$ denotes convolution in time with the frequency-dependent, thin-screen scattering response $h_\nu(t)$. Each microshot has a peak amplitude A_i Jy, drawn from a power law distribution with index $\alpha = -3$, and a Gaussian FWHM w_i, where W_0 (ms) is the envelope FWHM and the fractional microshot width w_i/W_0 is drawn from

$$\frac{w_i}{W_0} \sim \mathcal{U}(w_{\min},\, w_{\max})\,, \tag{1}$$

with $w_{\min}$ and $w_{\max}$ the minimum and maximum fractional microshot widths, respectively. t_i is the arrival time of the i-th microshot, which is distributed as $t_i \sim \mathcal{N}(t_0,\, \sigma_t)$, where t_0 is the

https://doi.org/10.1017/pasa.2026.10208 Published online by Cambridge University Press

Table 1. Model parameters used in `FIRES` as assumed inputs for representative simulations.

Parameter	Description	FRB 20191001A	FRB 20240318A
N	Number of microshots	100	100
A_i (Jy)	Peak amplitude of microshots; power law, $\alpha = -3$	[0.15, 15]	[0.015, 1.5]
t_i (ms)	TOA of ith microshot, $t_i \sim \mathcal{N}(t_0, \sigma_t)$	$\mathcal{N}(t_0, \sigma_t)$	$\mathcal{N}(t_0, \sigma_t)$
w_i (ms)	Microshot FWHM, sampled via Equation (1)	Sampled	Sampled
W_0 (ms)	Envelope FWHM	0.50	0.06
$w_{\rm min}$ (fraction of W_0)	Min. fractional microshot width	0.05	0.05
$w_{\rm max}$ (fraction of W_0)	Max. fractional microshot width	0.20	0.20
t_0 (ms)	Envelope reference TOA	Fixed	Fixed
ψ_0 (deg)	Mean intrinsic PA	20	0
σ_ψ (deg)	Microshot PA scatter	30	20
$\Pi_{L,0}$	Intrinsic frac. linear pol.	0.99	0.98
$\Pi_{V,0}$	Intrinsic frac. circular pol.	−0.05	−0.17
ν_τ (MHz)	Reference freq. for scattering and scintillation	1 000	1 000
τ_0 (ms)	Scattering timescale at ν_τ	1.78[a] ± 0.04	0.128[a] ± 0.005
α	Scattering index	−4.85[a] ± 0.3	−3.22[a] ± 0.005
ν_s (MHz)	Scintillation decorrelation bandwidth	2.05 ± 0.06	4[a] ± 0.2
t_s (s)	Scintillation timescale	300	300
$N_{\rm im}$	Number of images in scattering disk	5 000	5 000
$\theta_{\rm lim}$ (dimensionless)[b]	Angular limit of scattering disk	3	3
SEFD (Jy)	System equivalent flux density	1.2	1.4
$\delta\nu$ (MHz)	Channel bandwidth	1	1
δt (ms)	Time resolution	0.023	0.003

[a] Data from Scott et al. (2025).
[b] Defined in units of the characteristic scattering angle (see Section 2.2).

arrival time of the envelope, and

$$\sigma_t = \frac{W_0}{2\sqrt{2\log 2}}. \tag{2}$$

With per–microshot PAs $\psi_i \sim \mathcal{N}(\psi_0, \sigma_\psi)$, where ψ_0 is the mean intrinsic PA and σ_ψ is the standard deviation of the intrinsic microshot-to-microshot PA scatter, and fixed intrinsic fractional linear and circular polarisations $\Pi_{L,0}$ and $\Pi_{V,0}$, we write

$$\begin{aligned} D_Q[t,\nu] &= D_I[t,\nu]\cdot\Pi_{L,0}\cdot\cos(2\psi_i),\\ D_U[t,\nu] &= D_I[t,\nu]\cdot\Pi_{L,0}\cdot\sin(2\psi_i),\\ D_V[t,\nu] &= D_I[t,\nu]\cdot\Pi_{V,0}. \end{aligned}$$

2.1 Thin-screen scattering

We apply scattering via a discrete, causal impulse response per frequency channel. The continuous thin–screen scattering response is

$$h_\nu(t) = \frac{1}{\tau_\nu} e^{-t/\tau_\nu} H(t),$$

with Heaviside step $H(t)$ and timescale τ_ν. Let δt be the time resolution and let

$$n \equiv \left\lceil 5\,\frac{\tau_\nu}{\delta t} \right\rceil + 1$$

be the number of kernel samples. Then, the implemented kernel is the truncated, sum-normalised exponential

$$\begin{aligned} \mathrm{IRF}_\nu[k] &= \frac{e^{-k\delta t/\tau_\nu}}{\sum_{k=0}^{n-1} e^{-k\delta t/\tau_\nu}}\\ &= \frac{\left(1-e^{-\delta t/\tau_\nu}\right)e^{-k\delta t/\tau_\nu}}{1-e^{-n\delta t/\tau_\nu}}, \qquad k=0,\ldots,n-1, \end{aligned}$$

so that $\sum_{k=0}^{n-1}\mathrm{IRF}_\nu[k]=1$ (preserving flux), where k indexes the k-th discrete time sample. We zero-pad each time series on the right by $(n-1)$ samples, perform a linear (FFT) convolution, and truncate to the original timespan; any power beyond the simulated window is discarded.

The frequency-scaled scattering timescale is

$$\tau_\nu = \tau_0 \left(\frac{\nu}{\nu_\tau}\right)^\alpha, \tag{3}$$

with reference $\nu_\tau = 1$ GHz, frequency dependence α, and τ_0 the timescale at the reference frequency in milliseconds.

2.2 Scintillation

We include DISS as a multiplicative gain field $G(t,\nu)$ applied to all Stokes vectors. We generate a complex electric field $E(t,\nu)$ using `ScintillationMaker`[b] with four control parameters:

[b] https://github.com/SprengerT/ScintillationMaker/tree/main.

https://doi.org/10.1017/pasa.2026.10208 Published online by Cambridge University Press

the decorrelation bandwidth ν_s, characteristic timescale t_s, number of images drawn from the scattering disk $N_{\rm im}$, and the (dimensionless) angular extent of the scattering disk $\theta_{\rm lim}$, defined in units of the characteristic scattering angle (so that $\theta_{\rm lim} = 3$ corresponds to sampling the disk out to $\sim 3\sigma$). In our simulations we set $t_s = 300$~s, $N_{\rm im} = 5\,000$, and $\theta_{\rm lim} = 3.0$ to adequately sample the scattering disk and produce a realistic scintillation pattern while keeping computations manageable. ν_s is taken from Scott et al. (2025) when available, otherwise it is measured by fitting a single Lorentzian in the frequency power spectrum. The observed intensity gain is

$$G(t,\nu) \equiv \frac{\left|E(t,\nu)\right|^2}{\left\langle \left|E(t,\nu)\right|^2 \right\rangle_{t,\nu}},$$

so that $\langle G \rangle = 1$ over the simulated (t,ν) grid (preserving mean flux). The scintillated Stokes parameters are then

$$D_X^{(\rm DISS)}(t,\nu) = G(t,\nu)\, D_X(t,\nu), \qquad X \in \{I,Q,U,V\}.$$

For the large-batch simulations presented in the main text and appendices, scintillation is omitted to reduce computational cost. As discussed in Appendix E, tests including representative scintillation modulation patterns do not affect the results obtained in this work.

2.3 Noise

To mimic telescope noise, we add Gaussian noise to the dynamic spectra with

$$\varepsilon_X(t,\nu) \sim \mathcal{N}(0,\ \sigma_X)\,,$$

where σ_X is the noise level calculated from the radiometer equation,

$$\sigma_X = \frac{\rm SEFD}{\sqrt{n_{\rm pol}\delta\nu\delta t}}. \tag{4}$$

SEFD is the system equivalent flux density in Jy, $n_{\rm pol} = 2$ is the number of polarisations 'recorded,' $\delta\nu$ is the frequency resolution in Hz, and δt is the time resolution in seconds. For the ASKAP data considered here, this Gaussian approximation is appropriate. At substantially higher time and frequency resolution, however, the noise can become non-Gaussian (e.g. closer to a χ^2 distribution in minimally averaged baseband data), so alternative noise models may be required in future applications of `FIRES`. The observed Stokes are

$$D_X \leftarrow D_X^{(\rm DISS)} + \varepsilon_X, \qquad X \in \{I,Q,U,V\}.$$

2.4 Polarisation angles

We calculate the final PAs and their errors as performed by Day et al. (2020) and similarly debias the linear polarisation following (the typographically corrected) Equation (11) in (Everett & Weisberg 2001),

$$L_{\rm debias} = \begin{cases} \sigma_L \sqrt{\frac{L_{\rm meas}}{\sigma_L}^2 - 1}, & \frac{L_{\rm meas}}{\sigma_L} \geq 1.57 \\ 0, & \text{otherwise,} \end{cases}$$

except using σ_L instead of σ_I to accommodate cases where $\sigma_I \neq \sigma_Q \neq \sigma_U$. Further, we discard ψ where $L_{\rm debias} < 2\sigma_L$, along with those outside the on-pulse region, the minimum boxcar width that contains 95% of the flux in the pulse profile. If PA values are in a sequence of length < 5, then we also discard them.

3. Reproducing real FRB structures

Figure 1 shows the dynamic spectra of three stages of a `FIRES` simulation. Starting with a noiseless, unscattered FRB comprised of $N = 100$ microshots with a uniform distribution of widths ranging from 25–100 μs (see Equation 1); the FWHM of the full envelope is 0.5 ms. Then we add scattering, $\tau_{1\,\rm GHz} = 1.78$ ms and scintillation decorrelation bandwidth $\nu_s = 2.05$ MHz with characteristic timescale $t_s = 300$ s, and draw the phase screen with $N_{\rm im} = 5\,000$ images and truncation parameter $\theta_{\rm lim} = 3.0$. Then we add noise (SEFD = 1.2 Jy, see Equation (4); on-pulse S/N= 213), and finally compare to real CRAFT FRB 20191001A data reproduced from Scott et al. (2025) with `ILEX`[c] (on-pulse S/N= 194, corrected for RM= 53.47 rad m^{-2}). The simulated dynamic spectra are generated over a frequency range 751.5–900.5 MHz with 1 MHz resolution, and a time resolution of 0.023 ms chosen such that (the real) FRB 20191001A has a peak S/N$\sim$ 20. The frequency dependence for scattering is $\alpha = -4.85$. Post-processing measurements of the on-pulse polarisation fractions show $\Pi_L = 0.55$ and $\Pi_V = -0.05$. We assume that, intrinsically, each microshot is $\sim$100% polarised, and so we set $\Pi_{L,0} = 0.99$ and $\Pi_{V,0} = -0.05$ (similar to crab nanoshots, Hankins et al. 2016). Their PAs are drawn from $\mathcal{N}\left(20.0\,\text{deg}, 30.0\,\text{deg}\right)$. $\tau_{1\,\rm GHz}$ and α are taken from Table 2 of Scott et al. (2025), while the rest of the parameters are estimates made by-eye to mimic the properties of FRB 20191001A. The top PA panels include zoomed insets of the leading part of the burst to make the unresolved short-timescale PA structure easier to inspect. This initial comparison (Figure 1) is qualitative and intended to visually demonstrate that `FIRES` can generate realistic-looking bursts. The remainder of this work focuses on quantitative metrics that enable direct comparison between simulated and real FRBs. The full list of model parameters are presented in Table 1.

3.1 Polarisation angle variance

FRBs show variable PA properties (e.g. Luo et al. 2020; Mckinven et al. 2025), and when probed at high time resolutions, reveal systematic fluctuations (Nimmo et al. 2021; Hewitt et al. 2023; Scott et al. 2025). It has been suggested that the strength and duration of these PA microstructures may correspond to the magnetic field conditions in the emission environment (e.g. Scott et al. 2025), and so, disentangling intrinsic and extrinsic PA fluctuations is crucial for constraining emission models. Propagation effects such as scattering introduce frequency- and time-dependent effects that obfuscate intrinsic FRB structures, and so, determining under what conditions and which portions of the FRB dynamic spectra still contain original properties is also important.

Figure 1 shows that the PA of the simulated bursts is not constant, but varies with time, scattering timescale, and noise. We define two regions in the on-pulse phase (light-blue-shaded region); the leading region is from the onset of the on-pulse to and including the peak of the burst, and the trailing region is from the peak to the end of the on-pulse. As expected, scattering flattens the PA throughout the trailing region of the burst, reducing intrinsic variability (Li & Han 2003), while the leading region comparatively

[c] https://github.com/tdial2000/ILEX/tree/main.

https://doi.org/10.1017/pasa.2026.10208 Published online by Cambridge University Press

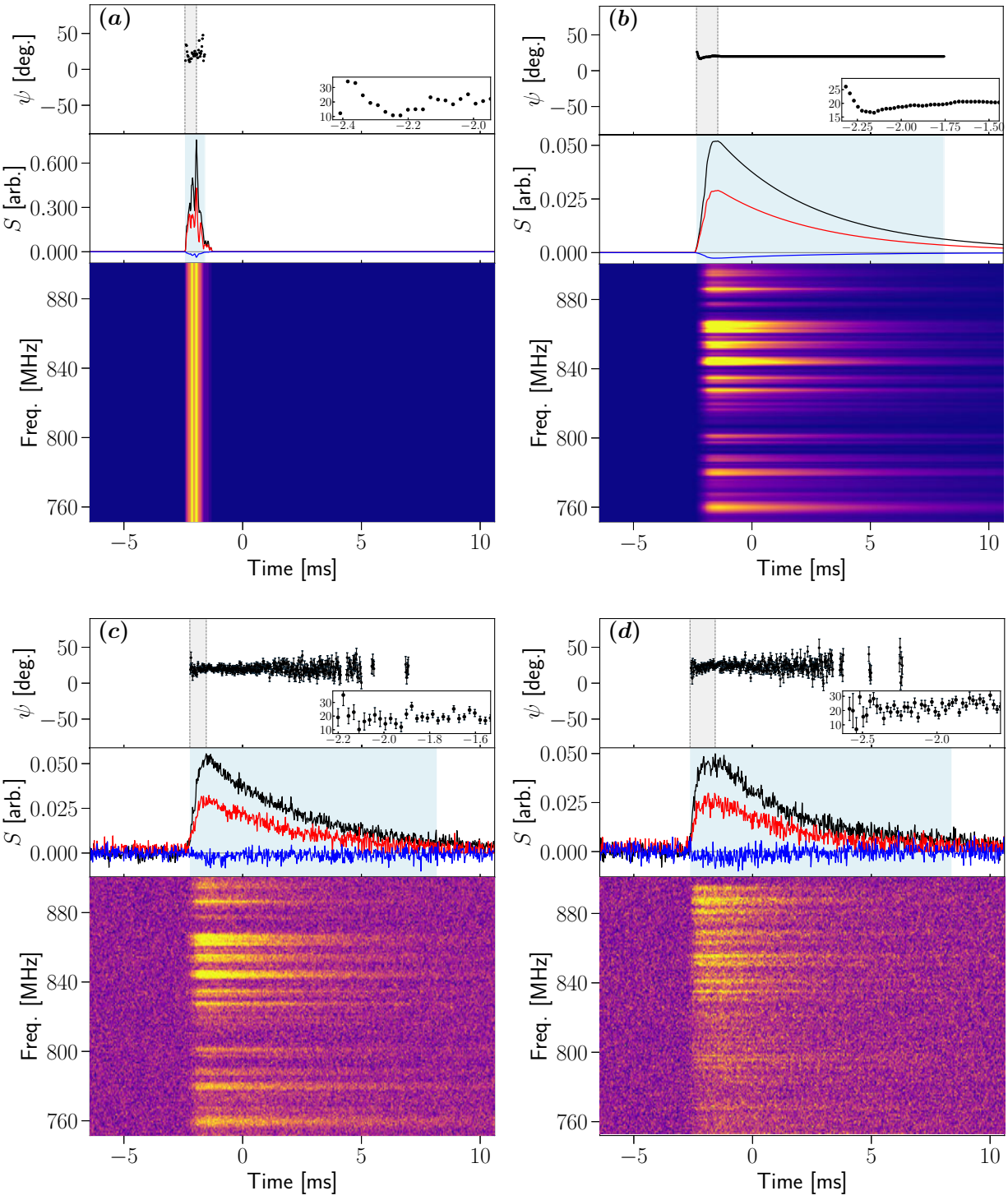


Figure 1. A `FIRES` recreation of FRB 20191001A. (a): a noiseless, unscattered FRB comprised of 100 microshots. The bottom panel is the time-frequency dynamic spectrum, the middle panel is the frequency-summed pulse profile (black = total intensity, red = linear polarisation, blue = circular polarisation), and the top panel is the polarisation angle profile. Each top panel includes a zoomed inset spanning the leading phase (from burst onset to the Stokes I peak) to highlight fine PA structure. (b): scattering timescale $\tau_{1\,\mathrm{GHz}} = 1.78$ ms and scintillation added to the top left plot. (c): noise added to the top right plot (on-pulse S/N= 180). (d): real FRB 20191001A data reproduced from Scott et al. (2025) (on-pulse S/N= 194, RM corrected from RM = 53.47 rad m^{-2}). The full list of parameters used are presented in Table 1 and are described in Section 2. The top panels show the polarisation angle, the centre panels show the pulse profile, and the bottom panels show the dynamic spectra. The blue shaded regions in the centre panels are the minimum boxcar width that contains 95% of the total flux in the pulse profile.

https://doi.org/10.1017/pasa.2026.10208 Published online by Cambridge University Press

remains largely unchanged. The introduction of noise dominates the macrostructure, introducing higher PA variance in the trailing edge.

To quantify the effects of scattering on PA in different burst regions, we introduce the metric,

$$\mathcal{R}_\psi = \frac{\mathbb{V}(\psi)}{\mathbb{V}(\psi_i)}, \tag{5}$$

where $\mathbb{V}(\psi)$ is the PA variance across the on-pulse phase and $\mathbb{V}(\psi_i)$ is the PA variance across the individual microshots that form the FRB. This parameter quantifies how much of the intrinsic microshot PA variance remains after taking their superposition. We can approximate the expected (noiseless) PA variance in deg.^{2} with,

$$\mathbb{V}_{\rm exp}(\psi) = \frac{\sigma_\psi^2}{N}\left(\frac{W_{\rm tot}}{w_{\rm tot}} - 1\right)\left(\frac{180}{\pi}\right)^2 \tag{6}$$

where $W_{\rm tot}$ and $w_{\rm tot}$ are the envelope and microshot FWHMs after scattering. We derive this expression in Appendix A. This approximation is only accurate for cases with high S/N and low σ_ψ. Substituting this into Equation (5), we can find the expected value of $\mathcal{R}_\psi$.

In Figure 2, we show how $\mathcal{R}_\psi$ modulates as a function of the input scattering timescale, τ_0, weighted by the input FWHM of the envelope, W_0, for different frequency bands and phase regions of a high S/N case of the simulated FRB shown in Figure 1(c). $\mathcal{R}_\psi$ exhibits three regimes, which are highlighted in the figure by light orange, light green, and light purple shaded regions, respectively. In the negligible-scattering regime, $\mathcal{R}_\psi$ remains constant with τ_0, since the scattering timescale is small compared to the intrinsic PA variation timescales (i.e. the width of each microshot). As τ_0 increases, $\mathcal{R}_\psi$ then decreases, as scattering blends random microshots together, reducing the variance. At very large τ_0, noise begins to dominate and variance increases. As expected, $\mathcal{R}_\psi$ in the lower frequency band is initially lower due to the frequency dependence of scattering, but becomes higher at large τ_0 once the PA is flattened by scattering and noise dominates. The trailing region follows the same trend but is more strongly affected by scattering, leading to a more rapid decline in $\mathcal{R}_\psi$. Similarly, the highest-quarter and full-band with total phase, also decrease as they become scatter dominated, but transition to the noise-dominated regime at larger τ_0 owing to their higher S/N.

By contrast, the leading edge consistently retains a larger fraction of the intrinsic PA variance at increasing scattering timescales. In high S/N cases, this makes the leading edge the most robust phase region for preserving information about the intrinsic PA structure, and therefore the most informative probe of the initial emission and generation conditions.

The black dotted line shows the expected value of $\mathcal{R}_\psi$ (Equation 6) in the noiseless regime and is in general agreement with all regions in the low-scattering, high-S/N limit.

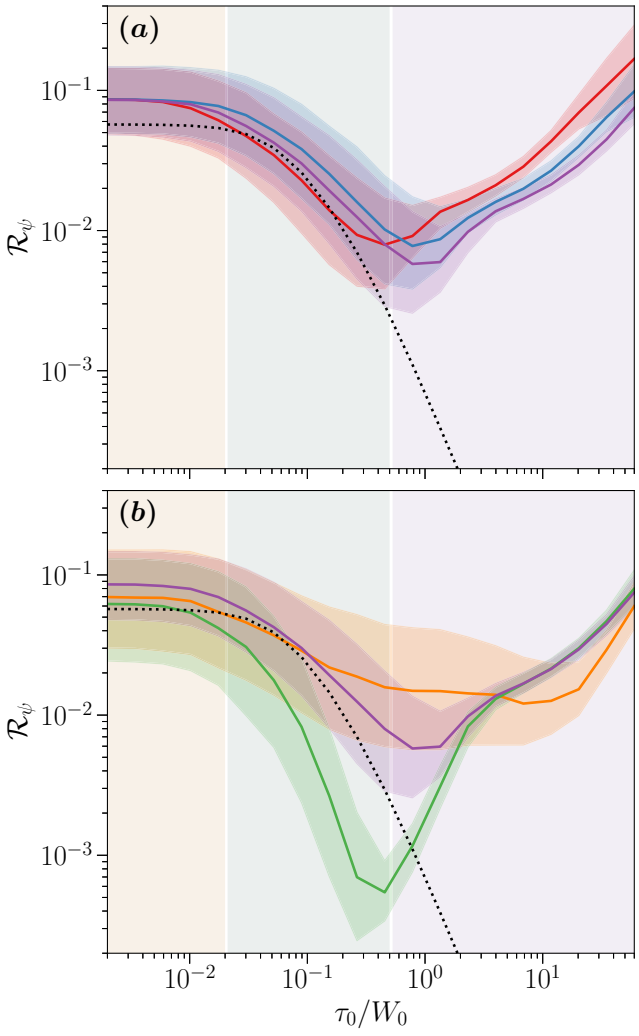


Figure 2. $\mathcal{R}_\psi$ (see Equation 5) versus τ_0 weighted by initial Gaussian envelope width, W_0, for a high S/N case of the mock FRB 20191001A (Figure 1(c)). The solid lines are the median value of 500 random FRB realisations at each scattering timescale, and the shaded regions represent the 16th and 84th percentiles of the realisations. The black-dotted line is the (noiseless) expected value from Equation (6). $\mathcal{R}_\psi$ exhibits three regimes, highlighted by the light orange, light green, and light purple shaded regions, respectively: a negligible-scattering regime where $\mathcal{R}_\psi$ remains approximately constant, an intermediate regime where scattering blends random microshots together and reduces the variance, and a large-scattering regime where noise dominates and the variance increases. (a): frequency band comparison; The red line is the contribution from the lowest quarter of the band, the blue line is the contribution from the highest quarter of the band, and the purple line is the contribution from the full band. (b): phase comparison; The orange line is the contribution from the first half of the burst, the green line is the contribution from the second half of the burst, and the purple line is the contribution from the entire burst. At $\tau_0/W_0 = 0, 60$, S/N $\sim 2300, 150$, respectively.

3.2 Linear polarisation fraction

FRBs generally exhibit high linear polarisation fractions (Sherman et al. 2024; Pandhi et al. 2024; Scott et al. 2025), and so it has been thought that all FRBs are intrinsically 100% linearly polarised, with any depolarisation or polarisation conversion occurring due to rotation measure (RM) scattering (Feng et al. 2022; Uttarkar et al. 2025). However, Sand et al. (2025) and Scott et al. (2025) show no correlation between scattering and polarisation fraction. Further, Scott et al. (2025) rule out depolarisation due to unresolved, random PA structures as there is no correlation between decreases in linear polarisation fraction and PA fluctuations. Sherman et al. (2024) also suggest that this case may be less significant than propagation effects.

Within the PSN framework, Figure 1 provides an illustrative example in which depolarisation arises from the superposition of microshots with differing PAs. The intrinsic microshot polarisation fractions are $\Pi_{L,0} = 0.99$ and $\Pi_{V,0} = -0.05$; however, when

https://doi.org/10.1017/pasa.2026.10208 Published online by Cambridge University Press

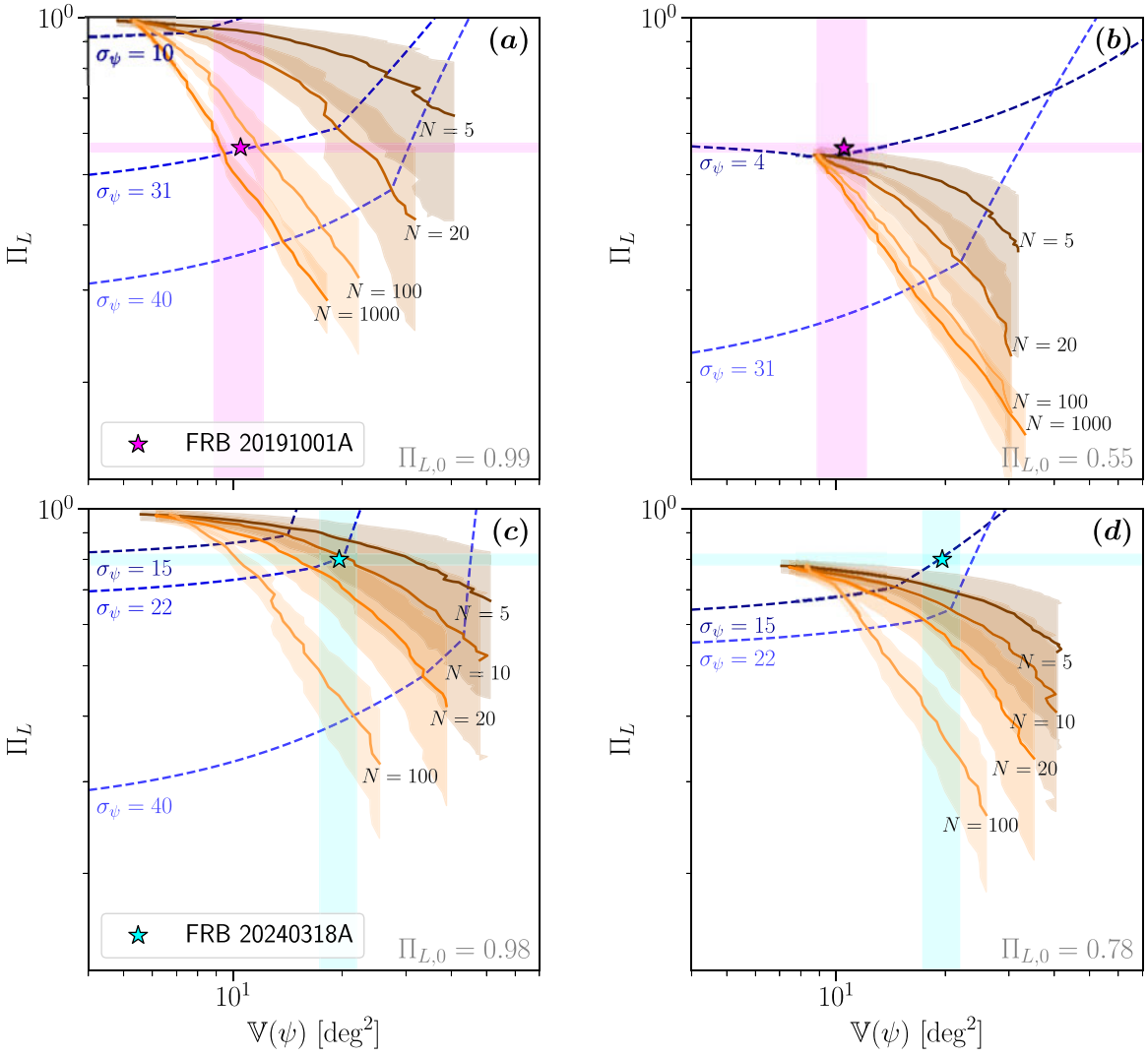


Figure 3. Measured linear polarisation fraction, Π_L, versus measured PA variance, $\mathbb{V}(\psi)$, as a function of the standard deviation of the intrinsic microshot PA, σ_ψ, for the leading phases of the mock FRB 20191001A (panels (a)–(b) with intrinsic linear polarisation fractions $\Pi_{L,0} = 0.99$ and 0.55, respectively) and FRB 20240318A (panels (c)–(d), $\Pi_{L,0} = 0.98$ and *red*0.78). For $N = 5$, 10, 20, 100, 1000 microshots, at each σ_ψ we generate 500 random realisations of each FRB with fixed S/N (FRB 20191001A: median $\sim$ 194; FRB 20240318A: median $\sim$ 110) and plot the medians of the Π_L and $\mathbb{V}(\psi)$ distributions as solid lines. The shaded regions mark only the 16th–84th percentiles of the Π_L distributions; they do not show percentile ranges in $\mathbb{V}(\psi)$. The magenta and cyan stars show the measured values for FRB 20191001A and FRB 20240318A, respectively (see Figures 1d and Figure B1b), with shaded bands indicating errors from off-pulse RMS noise. Blue dashed lines connect points of constant σ_ψ and are linearly extended using the slopes of their first and last segments (FRB 20191001A: $\sigma_\psi = 4°$, 10°, 31°, 40°; FRB 20240318A: $\sigma_\psi = 15°$, 22°, 40°).

superimposing $N = 100$ microshots with PAs sampled from a normal distribution with a standard deviation of $\sigma_\psi = 30°$, then $\Pi_L = 0.55$ as measured from the real FRB.

We illustrate this for the leading edge (see Section 3.1) of FRB 20191001A in Figure 3(a), (b) where we sweep $\sigma_\psi = 0$–45° for different values of N. In Figure 3, the shaded percentile regions quantify the spread in Π_L only; they do not represent the spread in $\mathbb{V}(\psi)$. Starting with $N = 5$ in Figure 3(a), the left-most point corresponds to $\sigma_\psi = 0°$, and the right-most point corresponds to $\sigma_\psi = 45°$. At $\sigma_\psi = 0°$ the intrinsic PA profile is completely flat, no depolarisation due to microshot superposition occurs and so $\Pi_L = \Pi_{L,0} = 0.99$. Here the only contribution to $\mathbb{V}(\psi)$ is from noise, as described by Equation (4) which determines the minimum $\mathbb{V}(\psi)$ for all values of N at $\sigma_\psi = 0°$. As we increase σ_ψ, $\mathbb{V}(\psi)$ increases and microshots with different PAs start overlapping, causing a reduction in Π_L. As we move to larger values of N, we increase the effective shot-rate ($N_{\rm eff}$ shots s^{-1}; see Appendix A) since the envelope width, W_0, remains constant. So, as N increases, microshots overlap more often and stronger depolarisation occurs for a given $\sigma_\psi > 0$. This also means that, since more averaging of PAs occurs, $\mathbb{V}(\psi)$ decreases for a given $\sigma_\psi > 0$. If we decrease $\Pi_{L,0}$, we decrease our signal in L and noise becomes more significant. So a decrease in $\Pi_{L,0}$ also corresponds to an increase in $\mathbb{V}(\psi)$ which we see when comparing to Figure 3(b) where we have reduced $\Pi_{L,0}$ to 0.55. Under the PSN model, we reproduce observable parameters and use these tracks to identify allowed combinations of N and σ_ψ for assumed $\Pi_{L,0}$, rather than to uniquely constrain a solution. The allowed regions are therefore conditional

https://doi.org/10.1017/pasa.2026.10208 Published online by Cambridge University Press

on the adopted microshot width and amplitude distributions (Appendix C.1, Appendix C.2).

We show the same analysis for FRB 20240318A in Figures 3(c), (d) and B1 using the parameters listed in Table 1. Post-processing measurements of the on-pulse polarisation fractions in Figure B1(b) show $\Pi_L = 0.78$ and $\Pi_V = -0.17$.

4. Discussion

Here, we first show that FIRES qualitatively reproduces FRB behaviour, then proceed to quantitatively constrain the allowed parameter space. In order to visually reproduce the properties of FRB 20191001A (Figure 1(c)), we adopt a 'single-component' envelope (Table 2 of Scott et al. 2025), implying an intrinsic FWHM $W_0 \sim 0.5$ ms given the measured scattering timescale $\tau_{1\,\mathrm{GHz}} = 1.78$ ms. As an illustrative example within the PSN model, we choose $N = 100$ microshots with intrinsic linear polarisation fraction $\Pi_{L,0} = 0.99$ arriving within W_0, for which matching the observed linear polarisation fraction requires $\sigma_\psi \sim 30°$ (Figure 3(a)). In this example, superposition of microshots with differing intrinsic PAs produces a time-variable PA profile, while scattering preferentially suppresses this variability on the trailing edge, broadly consistent with observations (Scott et al. 2025). While more rigorous statistical comparisons against the full HTR CRAFT sample remain for future work, the quantitative constraints below demonstrate the viability of the PSN framework.

4.1 Depolarisation mechanisms and parameter degeneracy

Scattering is not the sole mechanism that suppresses observable PA structure. Finite instrumental sampling further averages intrinsic PA fluctuations (Beniamini et al. 2022): when the sampling time δt exceeds the characteristic microshot separation, rapid PA variations are smoothed and depolarisation occurs, yielding an apparently flat PA profile even for relatively large σ_ψ. A similar degeneracy exists in the construction of the burst envelope itself: in our simulations the envelope is produced by varying the number of microshots with amplitudes, A_i, sampled from a power law and uniformly sampled widths, w_i, but comparable averaged behaviour could also arise from a constant number of shots with time-varying amplitudes, and different amplitude distributions and ranges, an effect that would likewise be smoothed by superposition and finite sampling (see Appendix C.1 and Appendix C.2).

In the PSN framework, depolarisation is set mainly by effective averaging: microshot overlap ($N\,w_i/W_0$), propagation smearing, and instrumental sampling. For $N\,w_i \gg W_0$, vector averaging in (Q, U) suppresses Π_L and flattens or disorders PA; for $N\,w_i \lesssim W_0$, shots are more resolved, so strong PA variation can coexist with comparatively high Π_L.

The Appendix and simulations show the same behaviour in $\Delta\psi \equiv \psi - \bar{\psi}$ versus $\Delta\Pi_L \equiv \Pi_L - \bar{\Pi}_L$ (Figure D1; Appendix D): the noiseless no-scattering case is a near-random walk about (0, 0), while a clear anti-correlation appears only when scattering is strong enough to enforce substantial averaging. With realistic noise, this anti-correlation is largely erased.

This interpretation is consistent with observations: more highly scattered bursts tend to show flatter PA (Scott et al. 2025), yet PA fluctuations do not robustly track L/I (Scott et al. 2025), and L/I shows no clear dependence on scattering timescale (Sand et al. 2025). Within PSN, these results imply that large-σ_ψ averaging is not the sole or primary depolarisation driver; instead, the observed behaviour reflects a coupled degeneracy among σ_ψ, N, τ, δt, A_i, w_i, and S/N, with a likely non-negligible contribution from external depolarising media along the propagation path (e.g. Uttarkar et al. 2026).

4.2 FRB case studies

These degeneracies are illustrated in Figure 3(b), where all simulations converge to identical Π_L and $\mathbb{V}(\psi)$ at $\sigma_\psi = 0$. Shifts in $\mathbb{V}(\psi)$ require changes in the effective S/N: increasing S/N reduces the measured PA variance, while decreasing the S/N of the linearly polarised intensity L (lowering $\Pi_{L,0}$) increases the contribution of noise to $\mathbb{V}(\psi)$. The measured values for FRB 20191001A (Figure 1(d)) therefore do not uniquely select a single intrinsic configuration, nor do they tightly determine the intrinsic linear fraction itself; rather, they define a model-dependent allowed region of $(N, \sigma_\psi, \mathbb{V}(\psi), \Pi_{L,0})$ space.

Under the PSN model with a set of assumptions about microshot width and amplitude distributions, Figure 3(a) shows that reproducing the observed properties of FRB 20191001A with intrinsically 100% polarised microshots ($\Pi_{L,0} = 0.99$, $\Pi_{V,0} = -0.05$) is compatible with intrinsic PA dispersions of order $\sigma_\psi \sim 31°$ when the number of microshots is $N \gtrsim 100$. This reflects efficient averaging of intrinsically misaligned PAs through microshot superposition, scattering, and finite instrumental sampling. However, once these averaging effects and the contribution of noise are accounted for, comparable levels of measured PA variance can also be obtained without invoking such large intrinsic dispersions. In particular, Figure 3(b) demonstrates that reducing the intrinsic linear fraction to the measured value of $\Pi_{L,0} = 0.55$ allows models with more modest PA dispersion ($\sigma_\psi \sim 4°$) and $N \lesssim 5$ to reproduce the observations. Larger values of N combined with slightly reduced $\Pi_{L,0}$ and smaller σ_ψ remain equally consistent. Taken together, the data for FRB 20191001A are best described by a broad, model-dependent region of parameter space in which modest intrinsic PA dispersion is compatible with the observed near-constant PA once instrumental resolution, propagation effects, noise statistics, and the assumed microshot-property distributions are properly incorporated.

By contrast, FRB 20240318A exhibits a significant, observable variable PA trend (Scott et al. 2025). Assuming a 100% polarised microshots ($\Pi_{L,0} = 0.98$, $\Pi_{V,0} = -0.17$), Figure 3(c) allows configurations with $N = 5$–20 and intrinsic PA dispersion $\sigma_\psi \sim 22°$. Relaxing this assumption to the measured $\Pi_{L,0} = 0.78$ shifts the allowed region toward fewer microshots, with Figure 3(d) favouring $N < 5$ and more modest PA dispersion ($\sigma_\psi \sim 15°$). A stricter interpretation of the resolved PA structure is that the data contain multiple independent PA excursions across the burst window; under that interpretation, very low-N solutions (e.g. $N < 5$) are less physically plausible in the PSN framework unless each observable excursion is produced by unresolved blends of multiple microshots. These solutions therefore occupy a different part of the same $(N, \sigma_\psi, \Pi_{L,0})$ space explored for FRB 20191001A, rather than requiring a fundamentally larger intrinsic PA dispersion. The observed PA variability therefore reflects a combination of reduced microshot averaging and intrinsic PA structure, rather than uniquely implying broader intrinsic PA distributions.

4.3 Model alternatives and interpretation

At the phenomenological level considered here, the main alternative to a multi-shot description is a single-shot or effectively

https://doi.org/10.1017/pasa.2026.10208 Published online by Cambridge University Press

single-component model in which the observed burst structure is generated within one emission episode rather than by superposition of many narrower shots. We do not rule out such alternatives in the present work. However, a single-shot picture appears to struggle more naturally to explain the rapid, μs PA variations seen in HTR bursts (e.g. Nimmo et al. 2022; Scott et al. 2025), whereas the PSN framework can reproduce qualitatively and quantitatively similar behaviour through the superposition, propagation, and sampling of many polarised microshots. We therefore view the current results as providing a first-order demonstration that the PSN model is viable over a broad parameter space, rather than as definitive evidence that it is uniquely required. Stronger support for, or against, the shot-noise interpretation will require a future statistical comparison of FIRES against the growing sample of HTR CRAFT FRBs and, ideally, against explicitly formulated alternative models.

4.4 Limitations and caveats

A key limitation of the present analysis is the use of PA variance as the primary diagnostic of intrinsic structure. Variance is not sensitive to how the PA varies in time, encoding neither coherence, intermittency, nor ordered swings. Consequently, distinct PA behaviours can yield similar $\mathbb{V}(\psi)$, particularly in noise-dominated or temporally averaged regimes (see Figure 2). Likewise, the present implementation treats the intrinsic PA structure primarily as stochastic microshot-to-microshot scatter, and so does not yet capture more complicated time-dependent PA evolution, such as coherent swings or other structured behaviour across the burst envelope. Structure-based metrics that explicitly quantify PA organisation (e.g. Scott et al. 2025) are therefore likely to provide a more informative and robust characterisation of intrinsic PA behaviour than variance alone. Future extensions of FIRES will incorporate such measures.

Finally, comparisons between FRB microstructure and Galactic pulsars such as the Crab must be interpreted cautiously. The extreme PA swings observed in Crab nanoshots occur on nanosecond timescales and would be strongly averaged out at the millisecond-to-microsecond resolutions of current FRB observations. As a result, present data probe only a temporally averaged manifestation of any underlying nanoshot structure, and unresolved Crab-like PA variability in FRBs cannot be ruled out. In addition, for very bright pulses observed at high time resolution, the inferred polarimetric variability can itself be affected by self-noise and small-number statistics when the averaging is insufficient (van Straten 2009). Apparent differences in polarimetric behaviour may therefore reflect observational limitations rather than fundamentally distinct emission physics.

4.5 Future model considerations

The present iteration of FIRES lacks several physical ingredients that will be incorporated into future versions:

- Multiple scattering and scintillation screens: Currently only a single thin-screen model is implemented, preventing realistic modelling of multi-path propagation and frequency-dependent scintillation structure.
- Thick-screen scattering: The code assumes an infinitely thin screen, whereas a volumetric or extended medium would alter temporal broadening and pulse-shape evolution.
- Generalised Faraday rotation: FIRES uses standard Faraday rotation, but cannot yet capture mode-coupling or birefringent effects expected in magnetised, relativistic plasmas.
- Structured intrinsic PA evolution and PA diagnostics: Future versions should incorporate more complicated time-dependent PA evolution, including coherent swings across the burst envelope, together with structure-based diagnostics that quantify PA organisation rather than variance alone.
- Alternative noise models: For the ASKAP data considered here, Gaussian noise is adequate, but at substantially higher time and frequency resolution the noise can become non-Gaussian. Future applications of FIRES should therefore generate the FRB and noise as electric fields at Nyquist resolution, allowing for noise to occupy a χ^2 distribution.
- Intrinsic spectral structure: Extending FIRES to include intrinsic spectral structure would improve the interpretation of its effects on FRB polarisation and flux variability.

5. Conclusions

We have introduced FIRES, an emission-mechanism-independent framework for modelling FRB dynamic spectra as the superposition of Gaussian microshots with varying PAs, followed by propagation effects and noise. Applied to CRAFT FRBs 20191001A and 20240318A, FIRES reproduces key polarimetric behaviours: scattering suppresses PA variability on burst trailing edges, while the leading edge preferentially preserves intrinsic structure. Depolarisation arises naturally from incoherent microshot superposition, with the relative contributions of N, σ_ψ, $\mathbb{V}(\psi)$, and $\Pi_{L,0}$ defining a degenerate but physically bounded parameter space.

For both FRBs, modest intrinsic PA dispersion remains viable once scattering, sampling, and noise are properly accounted for, and current data do not require fundamentally distinct intrinsic PA statistics between the sources. The leading-edge window and higher-frequency sub-bands provide the most robust access to intrinsic information. However, PA variance alone is an incomplete statistic and does not capture how PA varies in time; more structure-sensitive diagnostics are needed to fully characterise intrinsic PA evolution.

Future work will extend FIRES to incorporate multiple scattering screens, generalised Faraday rotation, and intrinsic spectral structure. Observationally, application to high-time-resolution, low-scattering FRBs will test whether FIRES can reliably recover intrinsic microshot properties and break current parameter degeneracies. Such observations will also directly test whether FRBs exhibit Crab-like nanoshot PA variability on unresolved timescales.

Acknowledgements. This research was supported by an Australian Government Research Training Program (RTP) Scholarship (https://doi.org/10.82133/C42F-K220). AB acknowledges support through project CORTEX (NWA.1160.18.316) of the research programme NWA-ORC, which is financed by the Dutch Research Council (NWO).

Data availability statement. ASKAP data used in this work are available online at https://doi.org/10.25917/1RG2-C612. The FIRES codebase and simulated data are available at https://github.com/JoelBalzan/FIRES.

References

Beniamini, P., & Kumar, P. 2020, MNRAS, 498, 651
Beniamini, P., Kumar, P., & Narayan, R. 2022, MNRAS, 510, 4654
Bera, A., & Chengalur, J. N. 2019, MNRAS, 490, L12
Bera, A., et al. 2024, ApJ, 969, L29
Cordes, J. M. 1976, ApJ, 210, 780
Day, C. K., et al. 2020, MNRAS, 497, 3335
Everett, J. E., & Weisberg, J. M. 2001, ApJ, 553, 341
Feng, Y., et al. 2022, Sci, 375, 1266
Gupta, V., et al. 2022, MNRAS, 514, 5866
Hankins, T. H., & Eilek, J. A. 2007, ApJ, 670, 693
Hankins, T. H., Eilek, J. A., & Jones, G. 2016, ApJ, 833, 47
Hankins, T. H., Jones, G., & Eilek, J. A. 2015, ApJ, 802, 130
Hazboun, J., et al. 2021, JOSS, 6, 2757
Hewitt, D. M., et al. 2023, MNRAS, 526, 2039
Hotan, A. W., van Straten, W., & Manchester, R. N. 2004, PASA, 21, 302
Jessner, A., et al. 2010, A&A, 524, A60
Li, X. H., & Han, J. L. 2003, A&A, 410, 253
Liu, X., et al. 2025, ApJ, 988, 175
Lorimer, D. R., Bailes, M., McLaughlin, M. A., Narkevic, D. J., & Crawford, F. 2007, Sci, 318, 777
Lu, W., & Kumar, P. 2018, MNRAS, 477, 2470
Luo, R., et al. 2020, Natur, 586, 693
Lyubarsky, Y. 2014, MNRAS, 442, L9
McKinnon, M. M. 2006, ApJ, 645, 551
Mckinven, R., et al. 2025, Natur, 637, 43
Melrose, D. B., & Macquart, J. P. 1998, ApJ, 505, 921
Nimmo, K., et al. 2021, NatAs, 5, 594
Nimmo, K., et al. 2022, NatAs, 6, 393
Osłowski, S., van Straten, W., Hobbs, G. B., Bailes, M., & Demorest, P. 2011, MNRAS, 418, 1258
Pandhi, A., et al. 2024, ApJ, 968, 50
Petroff, E., Hessels, J. W. T., & Lorimer, D. R. 2019, A&A Rev., 27, 4
Petroff, E., Hessels, J. W. T., & Lorimer, D. R. 2022, A&A Rev., 30, 2
Pleunis, Z., et al. 2021, ApJ, 923, 1
Rickett, B. J. 1975, ApJ, 197, 185
Sand, K. R., et al. 2025, ApJ, 979, 160
Scott, D. R., et al. 2025, arXiv e-prints, arXiv:2505.17497
Shannon, R. M., et al. 2025, PASA, 42, e036
Sherman, M. B., et al. 2024, ApJ, 964, 131
Snelders, M. P., et al. 2023, Nature Astronomy, 7, 1486
Uttarkar, P. A., et al. 2025, arXiv e-prints, arXiv:2503.19749
Uttarkar, P. A., et al. 2026, MNRAS, 545, staf1997
van Straten, W. 2009, ApJ, 694, 1413

Appendix A. Back-of-the-envelope derivation of the expected variance of the polarisation angle

We give a sanity check for the expected variance of the polarisation angle (PA) under the microshot model introduced in the main text. Let the envelope have FWHM W_0 (ms) and each microshot have FWHM w_i, with fractional width $w_i/W_0 \in [w_{\min}, w_{\max}]$. For an order-of-magnitude estimate we replace the fractional width by its mean

$$\bar{w} = \tfrac{1}{2}(w_{\min} + w_{\max}), \qquad w \equiv \bar{w}\, W_0.$$

Write $\kappa \equiv 2\sqrt{2\log 2}$ so that FWHM$\to\sigma$ via $\sigma = \mathrm{FWHM}/\kappa$. A thin-screen exponential scattering response with timescale τ_0 (ms) broadens Gaussian widths in quadrature,

$$\sigma_{W,\mathrm{tot}} = \sqrt{\sigma_W^2 + \tau_0^2}, \qquad \sigma_{w,\mathrm{tot}} = \sqrt{\sigma_w^2 + \tau_0^2},$$

with $\sigma_W = W_0/\kappa$ and $\sigma_w = w/\kappa$. The corresponding broadened FWHM measures are

$$W_{\mathrm{tot}} = \kappa\, \sigma_{W,\mathrm{tot}}, \qquad w_{\mathrm{tot}} = \kappa\, \sigma_{w,\mathrm{tot}}.$$

If N microshots occur within the envelope, the number that effectively contribute at any time scales with the broadened-width ratio. Defining

$$r \equiv \frac{w_{\mathrm{tot}}}{W_{\mathrm{tot}}} = \frac{\sigma_{w,\mathrm{tot}}}{\sigma_{W,\mathrm{tot}}}, \qquad N_{\mathrm{eff}} = N\, r,$$

and letting σ_ψ be the intrinsic single-shot PA scatter (radians), the rms PA scatter is

$$\psi_{\mathrm{rms}} \approx \frac{\sigma_\psi}{\sqrt{N_{\mathrm{eff}}}}, \tag{A1}$$

so the basic variance estimate is

$$\mathbb{V}_{\mathrm{exp}}(\psi) = \psi_{\mathrm{rms}}^2 = \frac{\sigma_\psi^2}{N\, r} = \frac{\sigma_\psi^2\, W_{\mathrm{tot}}}{N\, w_{\mathrm{tot}}}. \tag{A2}$$

When estimating fluctuations about the mean PA across the envelope, subtracting the mean introduces a degrees-of-freedom correction. Approximating the number of independent samples by $M \approx W_{\mathrm{tot}}/w_{\mathrm{tot}} = 1/r$ gives $(M-1)/M \approx 1 - r$, yielding

$$\mathbb{V}_{\mathrm{exp}}(\psi) = \frac{\sigma_\psi^2}{N\, r}\,(1-r) = \frac{\sigma_\psi^2\, W_{\mathrm{tot}}}{N\, w_{\mathrm{tot}}}\left(1 - \frac{w_{\mathrm{tot}}}{W_{\mathrm{tot}}}\right). \tag{A3}$$

Simplifying and converting to deg.,[2]

$$\mathbb{V}_{\mathrm{exp}}(\psi) = \frac{\sigma_\psi^2}{N}\left(\frac{W_{\mathrm{tot}}}{w_{\mathrm{tot}}} - 1\right)\left(\frac{180}{\pi}\right)^2. \tag{A4}$$

This corrected estimate tends to zero as scattering grows large ($r \to 1$). It ignores amplitude weighting, detailed temporal structure, and the full width distribution, but provides a rapid order-of-magnitude check. If needed for discretely sampled data with time resolution δt, one may downweight N_{eff} by $\min(1,\ \sigma_{w,\mathrm{tot}}/(\delta t/\kappa))$ to account for unresolved microshots.

https://doi.org/10.1017/pasa.2026.10208 Published online by Cambridge University Press

Appendix B. FRB 20240318A FIRES recreation and data

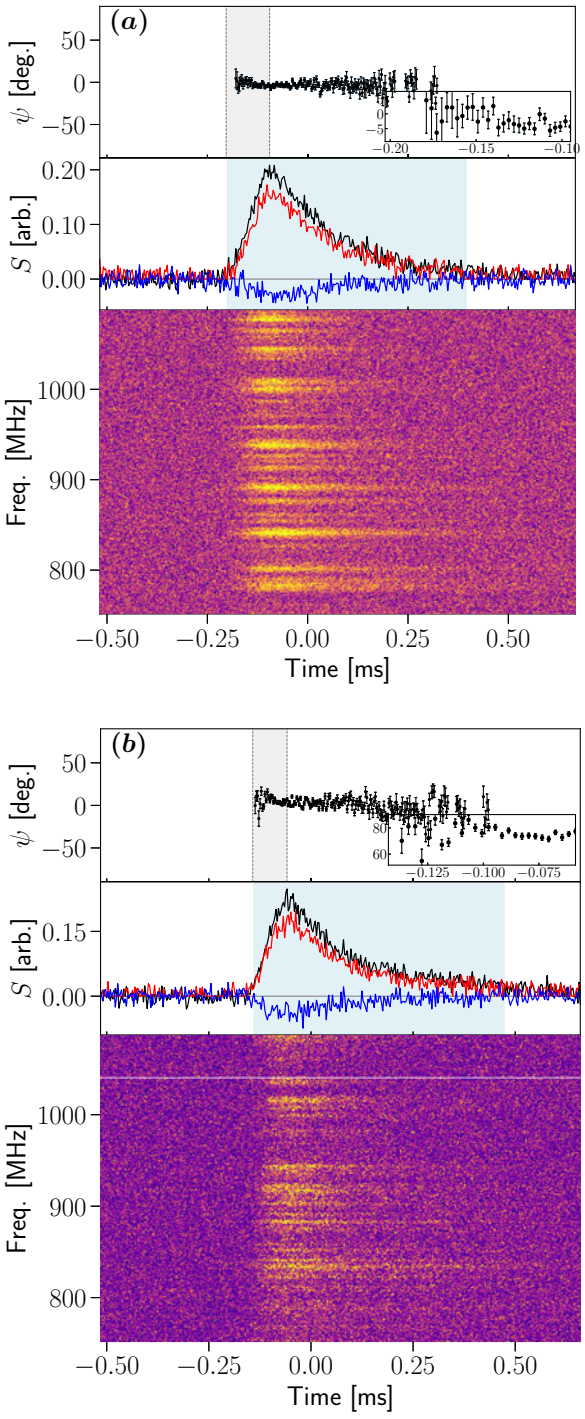


Figure B1. A FIRES comparison with FRB 20240318A. Top: A FIRES recreation of FRB 20240318A comprised of 100 microshots, $\tau_{1\,\mathrm{GHz}} = 0.128$ ms and scintillation (on-pulse S/N= 109). Bottom: real FRB 20240318A data reproduced from Scott et al. (2025) (on-pulse S/N∼ 110, RM corrected from RM=−48.03 rad m^{-2}). The full list of parameters used are presented in Table 1 and are described in Section 2. The top panels show the polarisation angle, the centre panels show the pulse profile, and the bottom panels show the dynamic spectra. The blue shaded regions in the centre panels is the minimum boxcar width that contains 95% of the total flux in the pulse profile.

Appendix C. FRB 20240318A parameter distribution comparisons

Appendix C.1. Amplitude distributions

Here we compare power law amplitude distributions with $\alpha = -1$ and -2. Figure C1 shows that the distributions aren't strongly distinguishable in the Π_L–$\mathbb{V}(\psi)$ plane, with the $\alpha = -1$ distribution producing slightly lower Π_L and $\mathbb{V}(\psi)$ at fixed σ_ψ and $N > 20$. This is because the $\alpha = -1$ distribution has more high-amplitude microshots that can dominate the polarisation properties. The differences between these distributions and the $\alpha = -3$ distribution used in Section 3.2 are relatively subtle compared to the effects of varying N and σ_ψ, and all three distributions can reproduce the observed properties of FRB 20240318A within the uncertainties. We thus adopt the $\alpha = -3$ distribution for our main analysis as it is more consistent with observed Crab GP energy distributions (Bera & Chengalur 2019).

https://doi.org/10.1017/pasa.2026.10208 Published online by Cambridge University Press

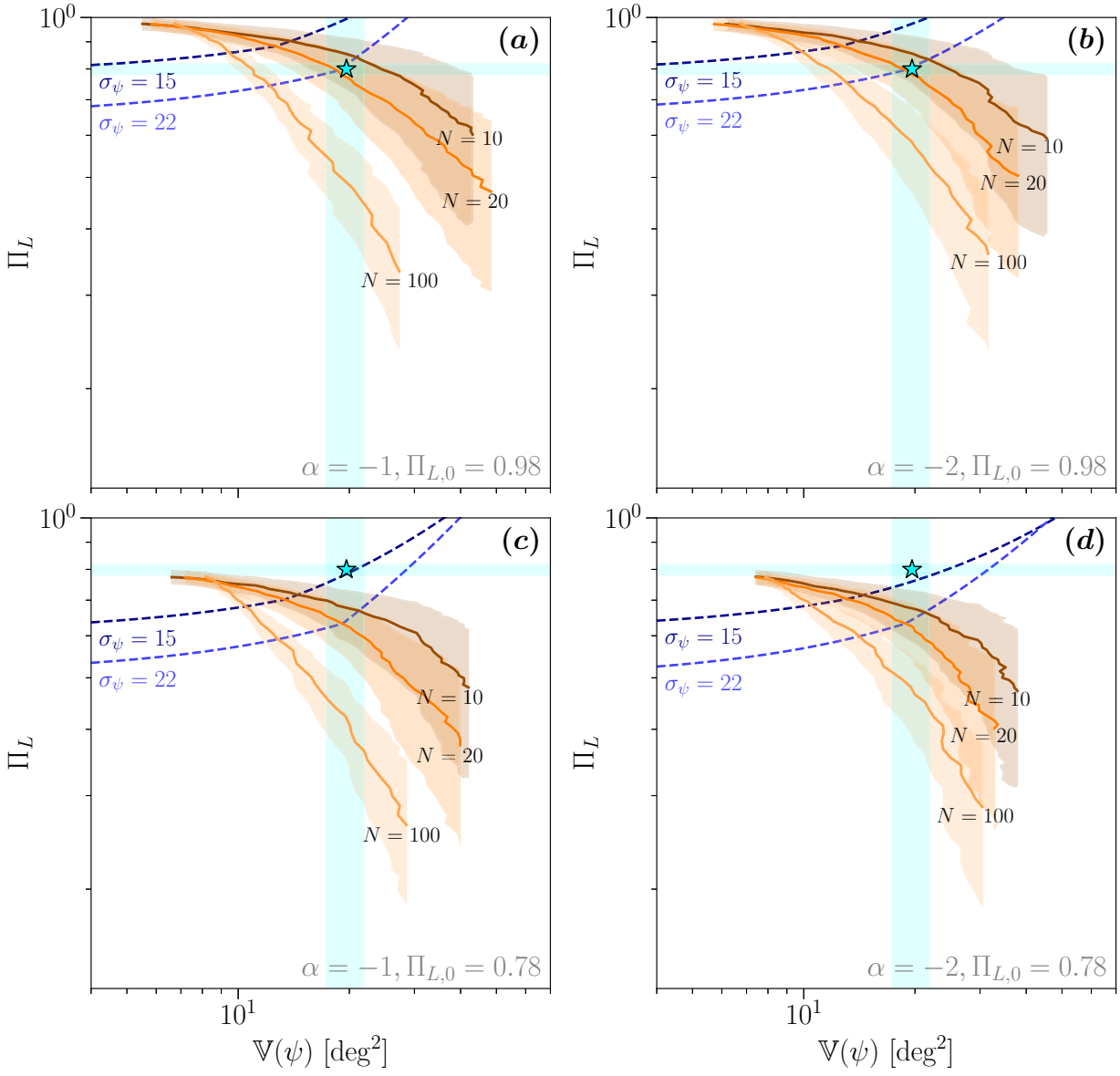


Figure C1. Measured linear polarisation fraction Π_L versus PA variance $\mathbb{V}(\psi)$ for mock FRB 20240318A power law amplitude distribution comparison. Left: $\alpha = -1$. Right: $\alpha = -2$. Top/bottom rows: intrinsic linear polarisation fraction $\Pi_{L,0} = 0.98$ and 0.78. Lines show medians for $N = 10, 20, 100$ (500 realisations per σ_ψ); shaded regions are the 16th–84th percentiles. Cyan star: measured FRB 20240318A (S/N$\sim$ 110) with off-pulse RMS uncertainty. Blue dashed lines: loci of constant σ_ψ.

Appendix C.2. Width distributions

We note that varying microshot widths introduces a degeneracy to varying shot amplitudes. Here we compare simulations with width distributions of 1–5% and 20–40% of the burst width. Figure C2 shows that the narrower width distribution produces a more extended track in the Π_L–$\mathbb{V}(\psi)$ plane, with the $N = 5$ track extending to higher σ_ψ values. The wider width distribution produces more compact tracks. This is because wider microshots are more likely to overlap and therefore produce more depolarisation and PA variance damping at fixed N and σ_ψ. This degeneracy makes it difficult to distinguish between a scenario with fewer, wider microshots and one with more, narrower microshots.

https://doi.org/10.1017/pasa.2026.10208 Published online by Cambridge University Press

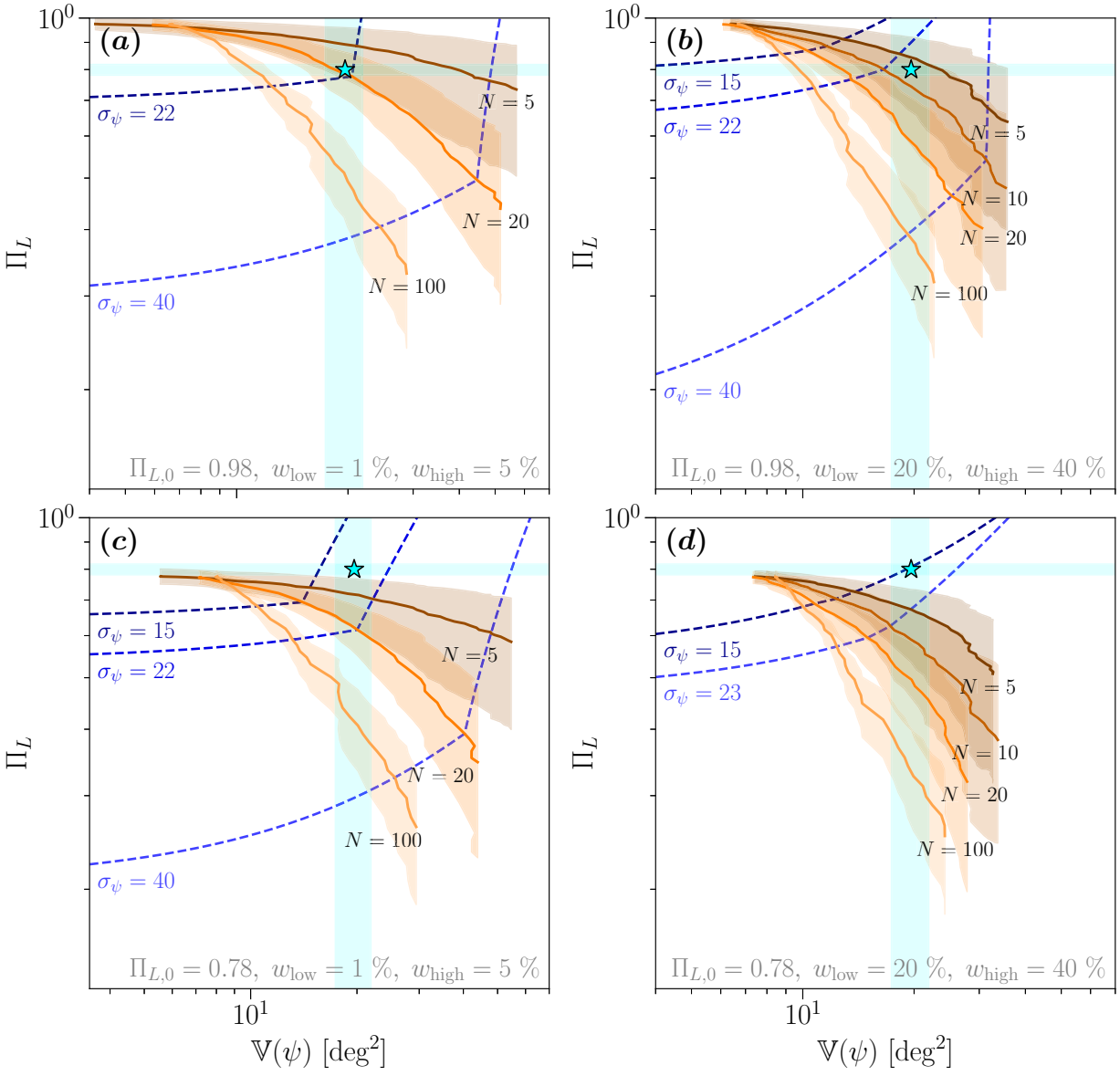


Figure C2. Comparison of width distributions for mock FRB 20240318A. Measured linear polarisation fraction Π_L versus PA variance $\mathbb{V}(\psi)$. Left/right columns: microshot fractional FWHM in [1%, 5%] and [20%, 40%]. Top/bottom rows: intrinsic microshot $\Pi_{L,0} = 0.98$ and 0.78. Lines show medians for $N = 5$, 10, 20, 100 (500 realisations per σ_ψ); shaded regions are the 16th–84th percentiles. Cyan star: measured FRB 20240318A (S/N$\sim$ 110) with off-pulse RMS uncertainty. Blue dashed lines: loci of constant σ_ψ. Some lines have been omitted for visual clarity.

Appendix D. Correlations between $\Delta\psi$–$\Delta\Pi_L$

Our simulations for $\Delta\psi \equiv \psi - \bar{\psi}$ versus $\Delta\Pi_L \equiv \Pi_L - \bar{\Pi}_L$ (Figure D1) show that depolarisation is governed by effective averaging (microshot overlap plus propagation/instrumental smoothing), rather than by intrinsic PA scatter alone.

In the noiseless scattered case ($\tau_0 = 0.128$ ms), there is a clear anti-correlation, consistent with incoherence in (Q, U) under strong overlap. The phase-space evolution in ($\Delta\psi$, $\Delta\Pi_L$) is also consistent with this picture: as effective averaging increases across the burst, the point cloud contracts toward the mean state (0, 0), reflecting suppression of both large PA excursions and large linear-polarisation offsets. Early-time bins can deviate because intrinsic structure is less averaged (Section 3.1). By contrast, in the noiseless no-scattering baseline ($\tau_0 = 0$), the correlation is weaker, indicating that intrinsic PA spread alone is insufficient to guarantee strong Π_L suppression. With realistic noise (S/N $\sim$ 110; L masked where $I < 2\sigma_I$), the relation disappears, implying that moderate intrinsic trends can be erased by measurement uncertainty and finite sensitivity. With noise added, the relation only begins to become visible at extremely high S/N.

Overall, the observed $\Delta\psi$–$\Delta\Pi_L$ behaviour is therefore controlled by a coupled parameter space – intrinsic PA scatter, number of emitting elements, overlap fraction (Nw_i/W_0), scattering timescale, sampling interval, amplitude/width distributions, and S/N – rather than any single parameter. This explains why flattened PA, PA variability, and low Π_L need not map one-to-one

https://doi.org/10.1017/pasa.2026.10208 Published online by Cambridge University Press

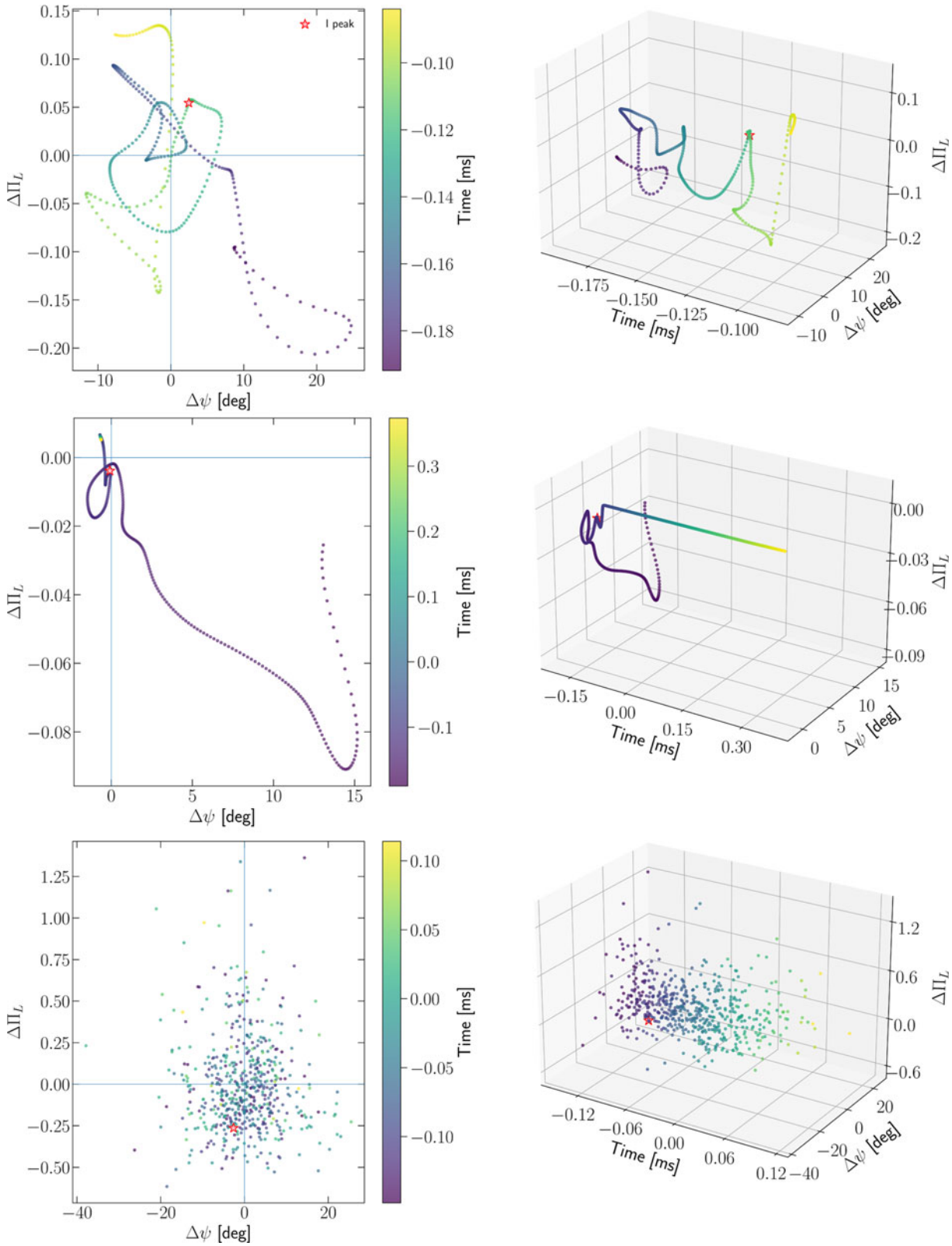


Figure D1. Correlations between polarisation-angle and linear-polarisation fluctuations for mock FRB 20240318A, demonstrating noise-dominated behaviour. Left column: $\Delta\psi \equiv \psi - \bar{\psi}$ versus $\Delta\Pi_L \equiv \Pi_L - \bar{\Pi}_L$, with points coloured by time. Right column: corresponding 3D visualisation with time as the explicit axis. Rows (top to bottom): no noise, no scattering ($\tau_0 = 0$ ms); no noise, with scattering ($\tau_0 = 0.128$ ms); and with scattering plus realistic noise (S/N$\sim$ 110). We have increased the sampling rate 10$\times$ compared to the main text to better inspect the tracks. Top: scattering plus noise (S/N$\sim$ 4 900), showing the correlation only becomes visible at unrealistically high sensitivity. Bottom: Real FRB 20240318A data from Figure B1b.

https://doi.org/10.1017/pasa.2026.10208 Published online by Cambridge University Press

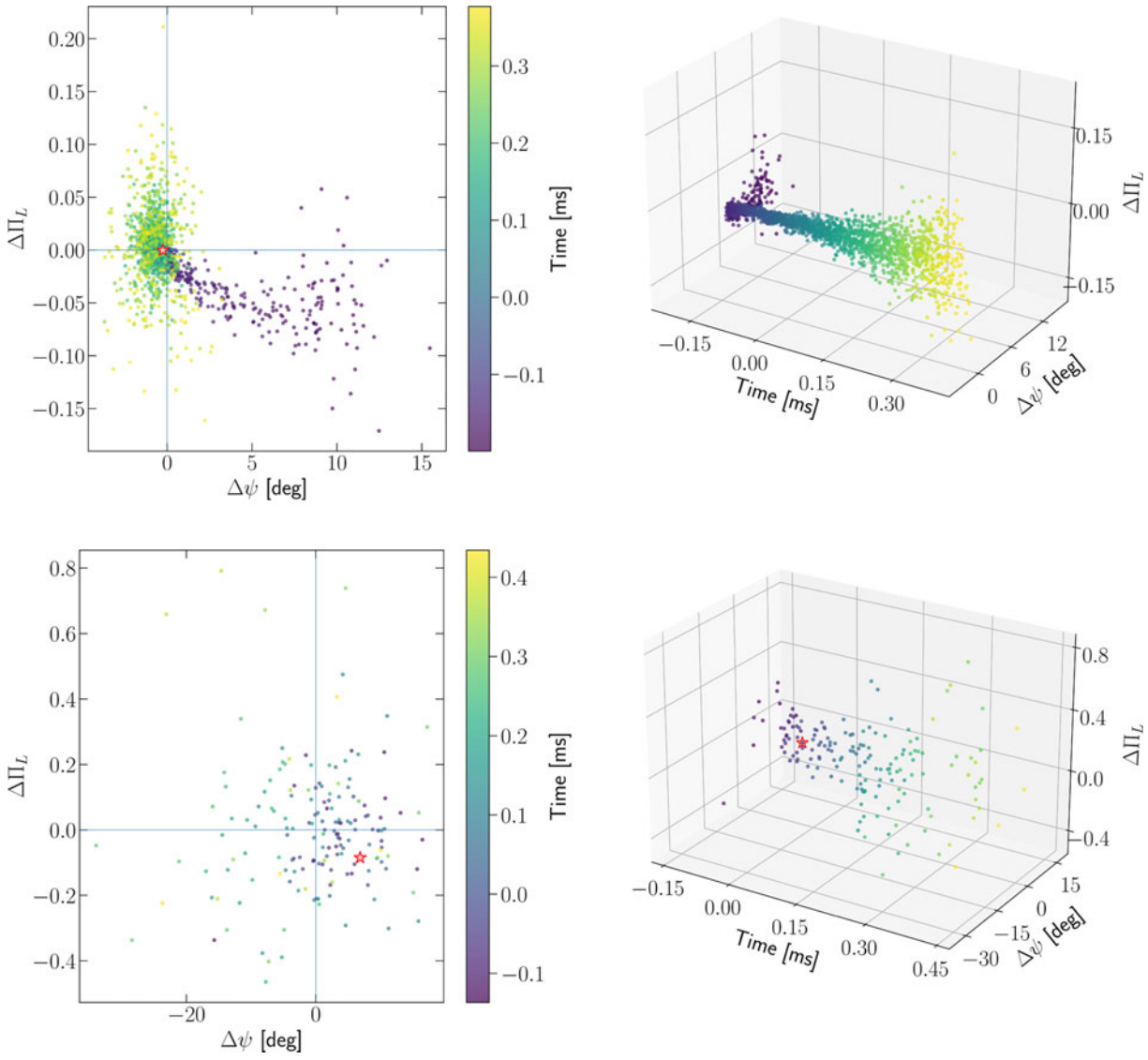


Figure D1. Continued.

across bursts, and why robust inference requires joint constraints on source microphysics and propagation/sensitivity effects (Section 4.1; cf. Sand et al. 2025; Scott et al. 2025).

Appendix E. Impact of spectral modulation on PA variance

To assess whether fine spectral structure affects the inferred PA variance constraints, we repeated the mock-burst simulations shown in Figure 3 after applying representative scintillation modulation patterns to the spectra using the procedure described in Section 2.2. We found that the resulting $(\Pi_L, \mathbb{V}(\psi))$ relations were visually indistinguishable from those obtained without scintillation, with no systematic shifts apparent beyond the intrinsic simulation scatter.

This behaviour is expected because any diffractive scintillation pattern is effectively static over the duration of an FRB burst – for Galactic scintillation at GHz frequencies, the characteristic scintillation timescale is many orders of magnitude longer than the millisecond burst durations considered here. While scintillation modulates the burst spectrum and local S/N, it cannot directly generate coherent time-dependent PA variations. We note that in principle, scintillation could indirectly affect PA results by introducing S/N-weighted frequency gaps that bias RM estimation; however, the RMs and scintillation strengths of the bursts in our sample are insufficient for this to be a concern.

While self-noise contributes to the uncertainty of spectral estimates, it does not produce correlated spectral modulation; instead, it manifests as uncorrelated variance in intensity estimates that averages down with the number of independent voltage samples within each integration. Stochastic wide-band impulse modulated self-noise (SWIMS; Osłowski et al. 2011) can produce temporally correlated noise variance when subpulse structure is resolved; however, since CRAFT data are Nyquist-sampled at 3 ns (Shannon et al. 2025), yielding $>10^3$ independent voltage samples per time bin at the time resolutions used here, any such cross-bin correlations in the Stokes parameters are significantly suppressed. Consequently, neither interstellar scintillation nor self-noise can generate the coherent time-dependent PA structure analysed in this work; self-noise may only contribute stochastic scatter to PA estimates.

https://doi.org/10.1017/pasa.2026.10208 Published online by Cambridge University Press